




Aerosol-into-liquid capture and detection of atmospheric soluble metals across the gas–liquid interface using Janus-membrane electrodes

Journal Article

Author(s):

Zhao, Yi-Bo; Cen, Tianyu; [Jiang, Fuze](#) ; He, Weidong; [Zhang, Xiaole](#) ; Feng, Xiaoxiao; Gao, Min; Ludwig, Christian; Bakker, Eric; [Wang, Jing](#) 

Publication date:

2023-03-07

Permanent link:

<https://doi.org/10.3929/ethz-b-000600985>

Rights / license:

[Creative Commons Attribution-NonCommercial-NoDerivatives 4.0 International](#)

Originally published in:

Proceedings of the National Academy of Sciences of the United States of America 120(10), <https://doi.org/10.1073/pnas.2219388120>



Aerosol-into-liquid capture and detection of atmospheric soluble metals across the gas–liquid interface using Janus-membrane electrodes

Yi-Bo Zhao^{ab}, Tianyu Cen^{cd}, Fuze Jiang^{ab}, Weidong He^{ab,e}, Xiaole Zhang^{ab}, Xiaoxiao Feng^{ab}, Min Gao^{ab}, Christian Ludwig^{cd}, Eric Bakker^f, and Jing Wang^{ab,1}

Edited by Alexis Bell, University of California, Berkeley, CA; received November 13, 2022; accepted December 28, 2022

The soluble fraction of atmospheric transition metals is particularly associated with health effects such as reactive oxygen species compared to total metals. However, direct measurements of the soluble fraction are restricted to sampling and detection units in sequence burdened with a compromise between time resolution and system bulkiness. Here, we propose the concept of aerosol-into-liquid capture and detection, which allowed one-step particle capture and detection via the Janus-membrane electrode at the gas–liquid interface, enabling active enrichment and enhanced mass transport of metal ions. The integrated aerodynamic/electrochemical system was capable of capturing airborne particles with a cutoff size down to 50 nm and detecting Pb(II) with a limit of detection of 95.7 ng. The proposed concept can pave the way for cost-effective and miniaturized systems, for the capture and detection of airborne soluble metals in air quality monitoring, especially for abrupt air pollution events with high airborne metal concentrations (e.g., wildfires and fireworks).

atmospheric soluble metals | aerosol-into-liquid | aerodynamic/electrochemical system | gas–liquid interface | air quality

Toxic and nonbiodegradable transition metals in the atmosphere released from extensive anthropogenic activities and natural emissions (1–3) are raising a significant threat to human health and the environment (4–6), in particular during acute air pollution accidents and emergencies (e.g., building fires and wildfires), which are now considered a poorly understood global problem requiring time-consuming efforts of sampling and analysis (7). For instance, the 2019 Notre-Dame Cathedral fire released a great amount of lead into the atmosphere, which was confirmed by the elevated Pb concentrations in honey samples collected after 3 mo (8). Children were subjected to the threat of lead poisoning in this acute pollution event (9). Wildfires also result in a significantly elevated level of transition metals (e.g., Pb and Cd) due to fire burning and metal remobilization (10, 11). These abrupt air pollution events might have long-term health effects by contaminating air, water, soil, and indoor environments (12). More importantly, the soluble fraction of particle-bound transition metals enhances the persistent toxicity and health effects (13–16), which is particularly harmful to humans due to its toxicity and bioaccessibility (17, 18), accounting for 0 to 80% of total metals in airborne particulate matter (PM) (19, 20). For instance, water-soluble transition metals in the accumulation mode have positive correlations with reactive oxygen species and oxidative stress (21, 22). Therefore, the detection of the soluble fraction in particle-bound transition metals is of great significance for public health, especially in order to give rapid responses to acute pollution events.

Monitoring by on-site, mobile, decentralized detection methods is a promising way to achieve rapid responses by eliminating sample transport, storage, and benchtop operation. In general, the common strategy is coupling different functional units (e.g., particle collection and measurement units) using benchtop or homemade instruments to determine the total airborne metals. Inductively coupled plasma mass spectrometry (ICP-MS) has been coupled with scanning mobility particle sizer (SMPS) to obtain size-resolved chemical information and particle characteristics simultaneously (23). Real-time detection of aerosol metals has been carried out using extractive electrospray ionization mass spectrometry (24). The combination of filter sampling and X-ray fluorescence analysis achieved the multimetal monitoring with a high time resolution, such as Cooper Xact 625i (25) and Horiba PX-375 (26). Nonetheless, these detection techniques such as X-ray fluorescence spectroscopy (XRF) require professional experiences and safety measures of radiative sources and are not able to distinguish the soluble fraction of metals in an oxidation state, though the health effects of metals are speciation-driven (27). A limited number of homemade on-site techniques have been developed based on electrochemical methods (28) or

Significance

Atmospheric soluble metals are strongly associated with adverse health effects, which require time-consuming efforts and great expense to complete sampling and detection steps due to their low concentrations and technology limitations. Here, we propose a concept of aerosol-into-liquid capture and detection that bridges free-flowing gas and static liquid phases to realize one-step capture and detection via the gas/liquid interface, unlike conventional strategies of sampling and detection units in sequence. The system presents effective capture of airborne ultrafine particles and detection of soluble metals at the nanogram level in a direct and cost-effective way, which is demonstrated by real-world samples and might be potentially applied in air quality monitoring, especially for abrupt air pollution events (e.g., wildfires and fireworks).

Author contributions: Y.-B.Z. and J.W. designed research; Y.-B.Z., T.C., F.J., W.H., X.Z., X.F., and C.L. performed research; Y.-B.Z. contributed new reagents/analytic tools; Y.-B.Z., T.C., F.J., W.H., X.F., M.G., C.L., E.B., and J.W. analyzed data; and Y.-B.Z., C.L., E.B., and J.W. wrote the paper.

The authors declare no competing interest.

This article is a PNAS Direct Submission.

Copyright © 2023 the Author(s). Published by PNAS. This article is distributed under [Creative Commons Attribution-NonCommercial-NoDerivatives License 4.0 \(CC BY-NC-ND\)](https://creativecommons.org/licenses/by-nc-nd/4.0/).

¹To whom correspondence may be addressed. Email: jing.wang@ifu.baug.ethz.ch.

This article contains supporting information online at <https://www.pnas.org/lookup/suppl/doi:10.1073/pnas.2219388120/-DCSupplemental>.

Published February 27, 2023.

well-established spectrophotometric techniques (27, 29), coupled with aerosol collection techniques. The state-of-the-art techniques are summarized in *SI Appendix, Table S1*. Previous studies mainly focused on total metal detection using the combination of the available aerosol collection with detection techniques, resulting in possible bulky coupling and extra uncertainty due to additional connections and sample preparation. However, studies in monitoring the soluble fraction of airborne soluble metals remain challenging and are scarce. Developing a more compact system for on-site detection of the soluble fraction of particle-bound transition metals, through integrating aerosol collection with detection techniques, still requires more novel coupling strategies and efforts.

Due to low power, high sensitivity, and selectivity for in situ measurements (30, 31), electrochemical detection is of great interest for sensing transition-metal ions, such as electrolytic deposition with subsequent electrochemical detection, nonelectrolytic preconcentration, and zero-current measurements (32). Among them, voltammetric methods are the most sensitive for transition-metal ion detection (33). The voltammetric determination of transition metals in PM_{10} was proved with a normalized deviation of less than 15%, compared to ICP-MS (34). For example, a Nafion/Bi-modified carbon electrode was used to determine Co(II) and Ni(II) in the aerosol collected on filters with limits of detection of 1 $\mu\text{g/L}$ and 5 $\mu\text{g/L}$, respectively (35). Electrochemical detection combined with aerosol collection techniques is a conventional and promising method to achieve the miniaturized platform of particle collection and detection. The aerosol collection techniques include passive collection (36) and capturing particles into liquid [wet collection surfaces (29, 37–40) and condensation growth method (41)]. Nonetheless, to avoid independent functional units in sequence, there is an emerging trend that

integrates collection and electrochemical detection in the same platform (42). The new coupling strategy is to create a dual-functional interface between particle collection and electrochemical sensing, by eliminating additional connections for sample transport, preprocessing, and storage.

In this study, we propose a new collection and sensing concept that allows for immediate sensing after particle collection via a gas/liquid interface. In this way, the mass transport of metal ions was enhanced by dissolving metals as close to the electrode surface as possible. Accordingly, a gold-coated polyacrylonitrile (PAN) nanofiber served as the aerosol-into-liquid electrode (AILE) with collection and sensing functions. It is a Janus membrane electrode with a virgin PAN surface on one side and a gold surface on the other side. A system integrating electrochemical methods with aerosol dynamics was developed to fulfill the aerosol-into-liquid concept via this membrane. In the proof-of-concept experiments, the integrated aerodynamic/electrochemical (IAE) system was examined using lab-generated lead aerosols and PM_{10} -like aerosols. The new concept achieved in the designed IAE system could afford a unique route toward the on-site monitoring of atmospheric metals and other additional components with a miniaturized size for rapid responses to abrupt pollution events.

Results

Capture and Sensing Strategy of the IAE System. The schematics and photo of the IAE system are shown in Fig. 1. The aerodynamic and electrochemical function modules were connected through the AILE electrode between the inertial impaction plate and the electrochemical cell (Fig. 1A). The AILE electrode supported by the electrolyte was facing the micrometer-sized nozzles delivering airflow at a jet-to-electrode distance of about 1 mm (Fig. 1B). By

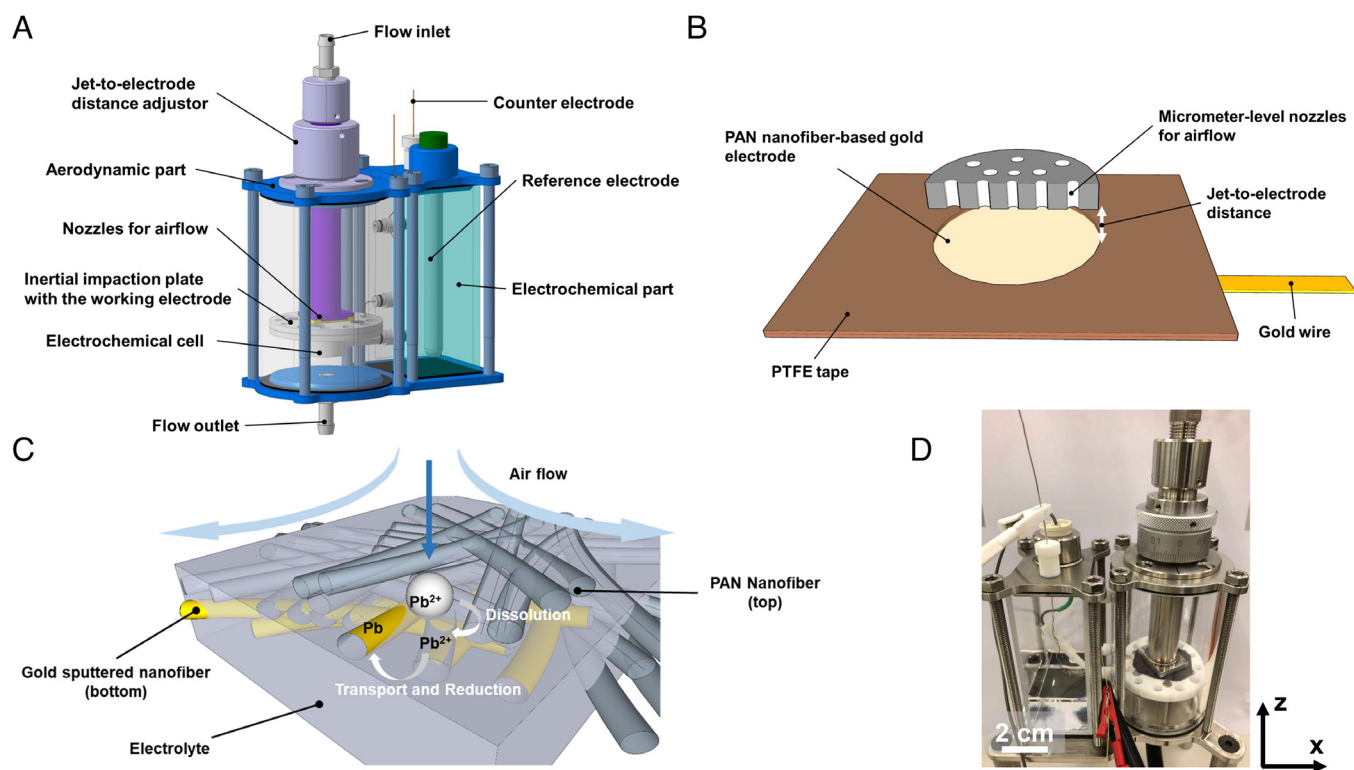


Fig. 1. Integrated aerodynamic/electrochemical (IAE) system for capturing and detecting airborne bioaccessible metals. (A) Schematic of the designed IAE system to achieve aerosol-into-liquid capture and detection, (B) detailed schematic of the gas/liquid interface separated by AILE electrode with a jet-to-electrode distance of around 1 mm, (C) schematic illustration of the aerosol-into-liquid collection and detection of particle-bound metal ions on the AILE electrode, (D) photo of the IAE system with a dimension of 100 mm \times 70 mm \times 100 mm in x -, y -, and z -axes.

joining the gas phase (air-jets containing particles) and the liquid phase (electrolyte), the AILE electrode worked as the impaction substrate for particles and the pores of the membrane served as liquid reservoirs to dissolve metals (Fig. 1C). The sensing strategy is to collect particles and dissolve metal ions on one side of the AILE electrode and perform electrochemical sensing reactions on the other side of the membrane electrode (gold-coated surface). In detail, particles are collected based on the inertial impaction and soluble metal ions from the particles are dissolved on electrolyte-soaked hydrophilic PAN nanofiber. Metal ions then diffuse vertically to the gold surface by mass transport for redox reaction (i.e., metal reduction and subsequent oxidation, see Fig. 1C). The metal reduction is used to accumulate metal ions on the electrode surface, while the oxidation is employed to obtain metal signals by producing an oxidation current. The IAE system was realized with a dimension of 100 mm × 70 mm × 100 mm in *x*-, *y*-, and *z*-axes, respectively (Fig. 1D).

Characterization of the AILE Electrode. The fabrication of the AILE electrode required several steps including electrospinning, hot lamination, and gold sputtering (Fig. 2A). Additional electrode assembly was also applied to support the soft electrode and the electrode area (SI Appendix, Fig. S1). The morphologies of the PAN nanofiber and the AILE electrode are shown in Fig. 2B and C. The PAN nanofibers without hot lamination were loose while the membrane became compact with a clear layer-by-layer structure after hot lamination. The diameter and porosity were quantified and the average diameters of pure PAN and gold-coated PAN were 225.5 ± 51.7 and 235.7 ± 54.1 nm, respectively (Fig. 1D). It indicates that hot lamination and gold sputtering

have a minor effect on the diameter size distribution. The porosity values of pure PAN and gold-coated PAN were 61.5% and 46.8%, respectively. The effect of the adsorption behavior of Pb(II) on the mass transport through the AILE electrode was also examined using ICP-MS. Then, 2.8% of the total Pb(II) at a relatively low concentration (10 μ M) was adsorbed on PAN nanofibers (Fig. 1E), and the average adsorption capacity was 3.45 μ g/g, which indicates insignificant adsorption of Pb(II) on PAN nanofibers and its minor effect on sensing performance. Adsorption and desorption were fast since the concentration of lead in the solution was not changed much in each phase (Fig. 2E). A relatively stable concentration of lead in the repeated adsorption revealed that the AILE electrode was reusable without much effect of Pb(II) adsorption.

The water wettability of the PAN nanofiber was analyzed via water contact angle, which was about 37° (43). The PAN membrane was hydrophilic and had an affinity for water to form a nonporous liquid-saturated membrane, which was desirable for separating the liquid phase from the gas phase without disturbance from a fast-moving gas flow. A gold rotating disk electrode (RDE) was used to investigate the Pb redox reaction in steady states. The roughness factor (~ 1.71) of the gold RDE was obtained by stripping a gold oxide layer in 0.5 M H_2SO_4 and the conversion factor of $390 \mu\text{C cm}^{-2}$ was used (44), whereas the roughness factor of the PAN nanofiber-based gold electrode was 3.92 (SI Appendix, Fig. S2). Considering the porosity of the PAN nanofiber-based gold electrode of 46.8%, which resulted in a smaller geometric area, the roughness factor of the gold surface could increase up to 7.37. It indicated a rougher gold surface of the PAN nanofiber-based gold electrode compared to gold RDE (45).

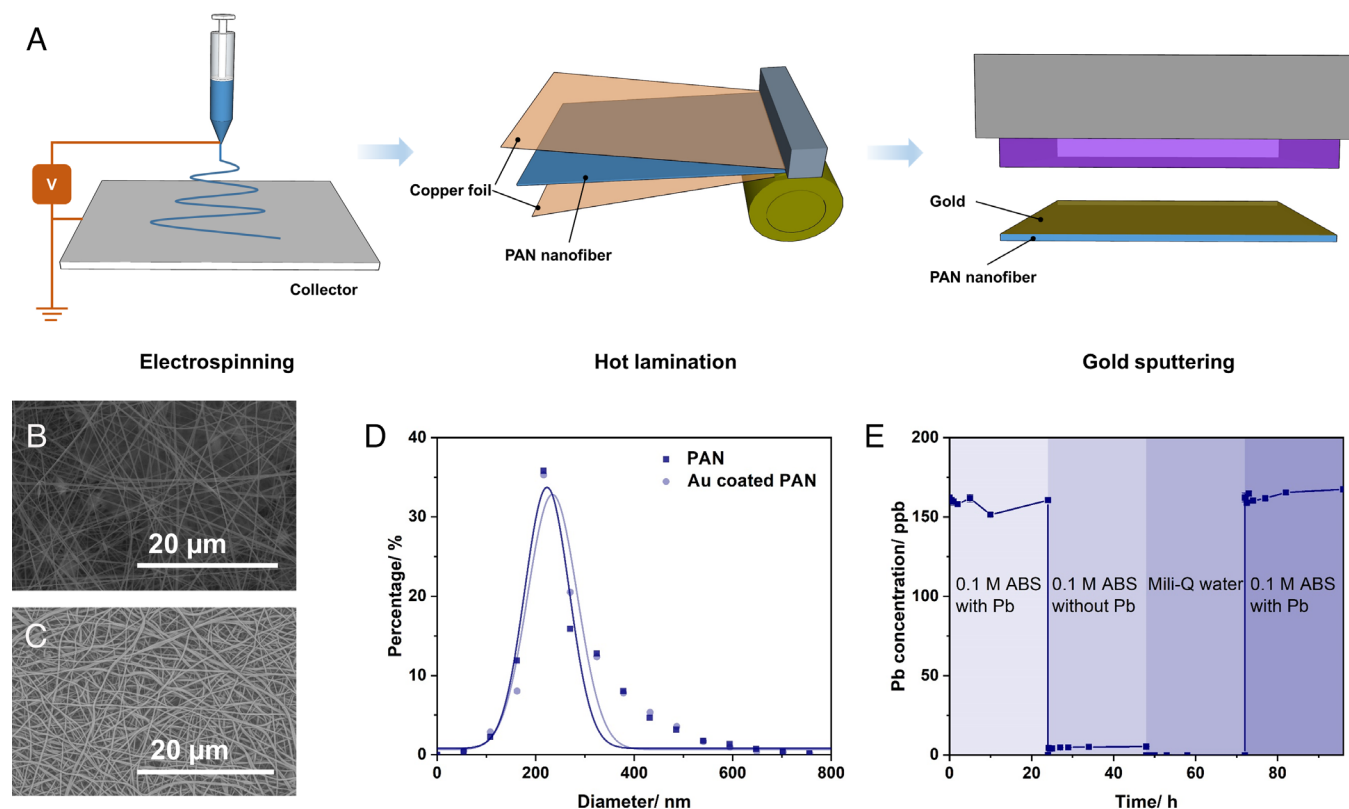


Fig. 2. Fabrication and characterization of the AILE electrode. (A) Schematic illustration of fabricating the AILE electrode, (B) scanning electron microscopy (SEM) image of the PAN nanofiber after hot lamination, (C) SEM image of the gold surface of the AILE electrode, (D) diameter size distributions and the Gaussian fitting of the PAN nanofiber, and the AILE electrode, (E) adsorption of Pb(II) onto the PAN nanofiber, desorption of Pb(II) from the PAN nanofiber, and adsorption of Pb(II) onto the PAN nanofiber as a function of submersion time (adsorption experiment: 40 mg PAN nanofiber in 30 mL 0.1 M acetate buffer solution (ABS) (pH 4.45) containing 10 μ M Pb(II) for 24 h; desorption experiment: the PAN nanofiber was transferred into 30 mL ABS for 24 h and then into 30 mL Milli-Q water for 24 h).

Electrochemical Characterization and Detection of Pb(II) in the Liquid Phase. The detection of atmospheric soluble metals is a liquid-based method, so the gold RDE and PAN nanofiber-based gold electrodes were employed to examine the feasibility of sensing Pb(II) in the liquid phase. As shown in Fig. 3A, the oxidation and reduction potentials of Pb(II) were 0.4 to 0.6 V and 0.3 to 0.5 V, respectively. The onsets of the oxygen reduction and hydrogen evolution were at 0.4 V and -0.1 V, respectively (Fig. 3A and *SI Appendix, Fig. S3*). Therefore, the deposition potential was set at -0.2 V, to avoid competitive hydrogen evolution reactions in view of the limited number of active sites on the gold surface, despite the fact that hydrogen evolution reaction has limited effects on Pb deposition (46). The gold rotating disk electrode (RDE) was considered a flat bare gold surface to detect metal ions under tunable conditions. In particular, a high rotation rate (i.e., 1,600 rpm) allowed the continuous deposition of metal ions on the electrode with constant mass transport, to simulate the presence of metal ions with high concentrations. Fig. 3B indicated that there were one underpotential deposition and two overpotential depositions of lead on the gold surface. In general, the relationships between concentrations and integrated charge were quite linear (*SI Appendix, Figs. S4–S6*), which indicated that gold as a sensing material was capable of detecting Pb(II) in the liquid phase.

For the AILE electrode, the oxidation potential range of Pb(II) was 0.25 to 0.60 V (*SI Appendix, Fig. S5*). It should be noted that the limit of detection in the liquid phase depends on the deposition (reduction) time in certain ranges (47), which means a longer deposition time results in more deposited metals and a lower limit of detection. The conversion of stripping charges to Pb concentration revealed that $0.204 \pm 0.024\%$ Pb(II) was reduced on the gold surface without stirring in the solution after 5 min deposition (Fig. 3C). According to the square wave voltammetry (SWV)

signals, the peaks fell into the range of 0.3 to 0.6 V (Fig. 3D). The relationship between electrode area and current peak suggested that a smaller electrode area on the mm² scale was more preferable due to slower changes in the current peak value in comparison of the electrode area ($0.11 \mu\text{A}/\text{mm}^2$) (*SI Appendix, Fig. S7*), suggesting the signal obtained from a smaller area of the electrode could be comparable to that obtained from a large electrode. Fig. 3E illustrated the detection performance with a relatively low concentration of metal ions ($<1.2 \mu\text{M}$) in the presence of oxygen ($R^2 > 0.99$). The limit of detection was 79.2 nM, according to the equation Limit of Detection (LOD) = $3 \delta/S$, where δ is the SD of the background signal, and S is the ratio of the Pb concentration to the current signal. The interference study was conducted with different ions, and the range of detection ratio was 80 to 130% (Fig. 3F). Particularly, Cu(II) might interfere with the Pb signal by the replacement of Pb deposition (48). Overall, the AILE electrode was sensitive and selective for detecting Pb in the liquid phase.

Collection Efficiency and Particle Loss of the IAE System.

The cutoff diameter at 3.0, 5.0, 7.1, and 7.9 L/min was about 300, 150, 80, and 50 nm, respectively (Fig. 4A). The collection efficiency increased with a higher flow rate, and it mainly affected the collection of particles smaller than 300 nm. The setup for determining the collection efficiency of the system was shown in *SI Appendix, Fig. S8*. The collection efficiency was not strongly influenced by the nozzle-to-plate distance especially when it was smaller than 1.5 mm (Fig. 4B). The vertical deformation of the AILE electrode with different nozzle-to-plate distances could play a role in the effect of the nozzle-to-plate distance on the collection efficiency. Pore number and size also affected the collection efficiency, and a higher velocity caused by the lower porosity of the nozzle plate resulted in higher collection efficiencies (Fig. 4C).

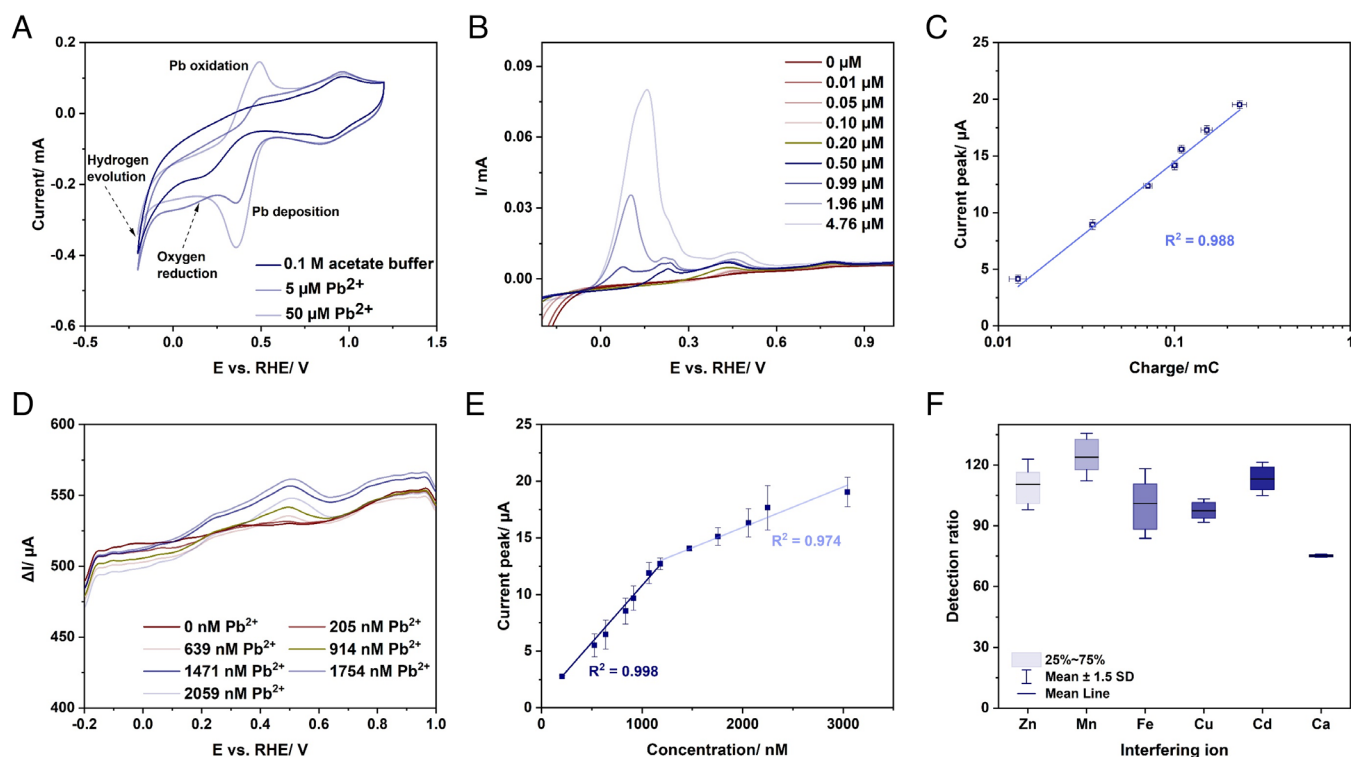


Fig. 3. Characterization and sensing performance of the AILE electrode. (A) Cyclic voltammetry in 0.1 M acetate buffer (pH 4.45) without and with Pb(II) at 100 mV/s in a three-electrode system under air, (B) RDE experiments using ASV on the stripping current as a function of concentration gradients of Pb(II) at 1,600 rpm in 0.1 M acetate buffer in an Argon-saturated environment, (C) relationship between the stripping charge using anodic stripping voltammetry and the current peak using square wave stripping voltammetry with an AILE electrode ($\varnothing = 16 \text{ mm}$), (D) responses upon concentration gradients of Pb(II) for the AILE electrode, (E) relationship between the current peak (in the range of 0.3 to 0.6 V) and the Pb(II) concentration gradients, (F) selectivity of the AILE electrode toward $1 \mu\text{M}$ Pb(II) in the presence of 50 times higher concentration of other metal ions [Zn(II), Mn(II), Fe(III), Cu(II), Cd(II), and Ca(II)], respectively.

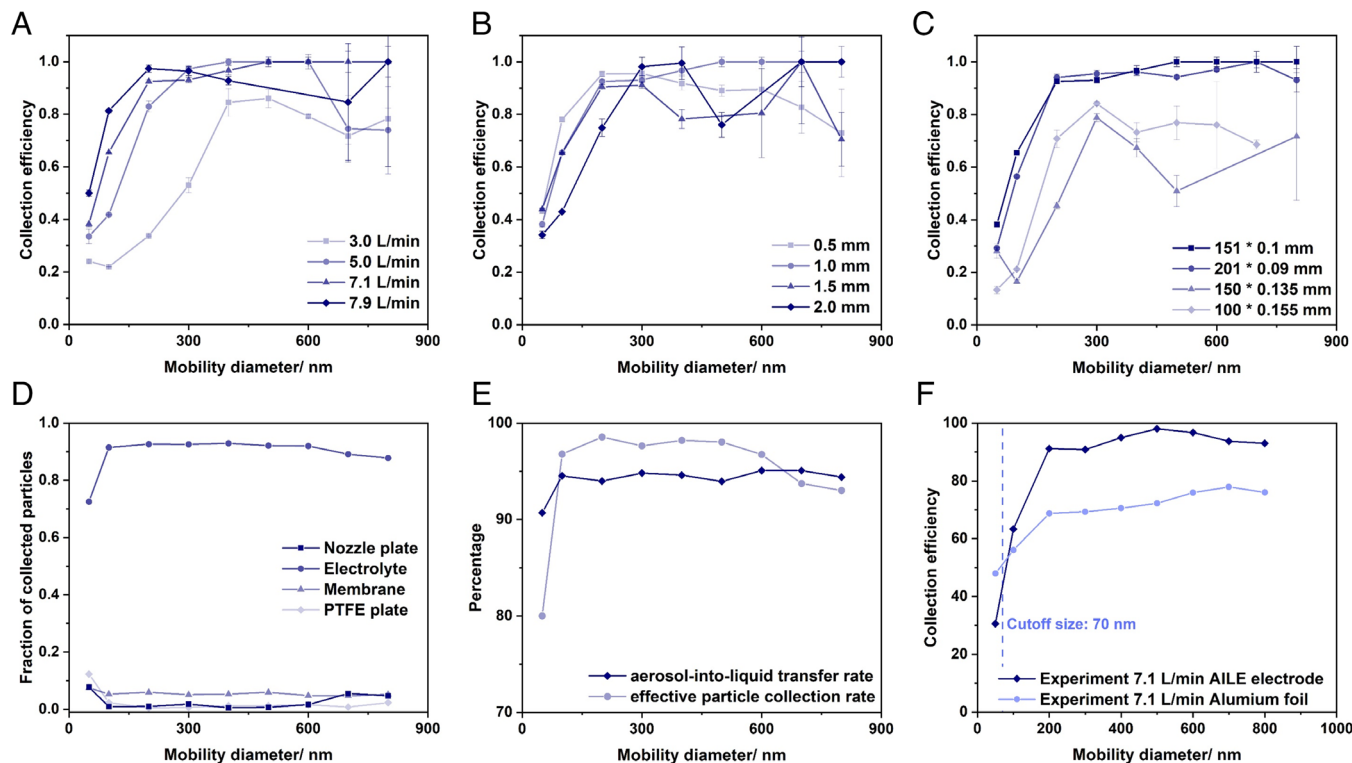


Fig. 4. The integrated aerodynamic/electrochemical (IAE) system and its collection performance. (A) Collection efficiency of the IAE system as a function of different flow rates (1 wt% NaCl), (B) collection efficiency of the IAE system as a function of different nozzle-to-plate distance (1 wt% NaCl), (C) collection efficiency of the IAE system as a function of different nozzle number and pore size (1 wt% NaCl), (D) percentage of the size-resolved particle collection on PTFE plate, membrane (AILE electrode), electrolyte, and nozzle plate, (E) particle losses and aerosol-into-liquid transfer rate of the IAE system using monodisperse NaCl particles selected by DMA after 2 h collection at 7.1 L/min, (F) comparison of the collection efficiency using an AILE electrode as the impactation plate with that using an aluminum foil.

Specifically, given the same volumetric flow rate, 0.59% and 0.64% porosity led to a smaller cutoff size of around 70 nm and maximum collection efficiency up to 100%, while 1.05% and 0.93% porosity caused the larger cutoff size of 200 nm and maximum collection efficiency of about 80%. It should be noted that the number of re-aerosolized water droplets from the electrode could affect the measured collection efficiency of particles larger than 300 nm because the number of challenge particles decreased with larger particle sizes. The collected particles on different parts of the system were investigated to estimate the effective particle collection rate and aerosol-into-liquid transfer rate (Fig. 4D and E). Particles larger than 100 nm were well collected in the electrolyte by diffusing through the AILE electrode, and particle loss of smaller particles became significant likely due to particle diffusion in the airflow hitting the nozzle plate and Polytetrafluoroethylene (PTFE) plate (Fig. 4D). The effective particle collection rate was above 80% and the aerosol-into-liquid transfer was above 90%, which demonstrated a minimum particle loss and proved the feasibility of the aerosol-into-liquid concept (Fig. 4E). Here, the effective particle collection rate was defined as the fraction of collected particles on the AILE electrode and subsequently diffusing to the electrolyte, while the aerosol-into-liquid transfer was the fraction of the collected particles diffusing into the electrolyte. Fig. 4F showed that the collection efficiencies curve for particles larger than 200 nm reached a stabilized plateau, suggesting that the soft membrane surface used in this system reduced the solid particle bouncing significantly, which occurs with particles larger than 200 nm in many studies of designed impactors (49, 50).

The whole system was operated at relatively low pressures (e.g., 0.85 atm), and particles with a cutoff diameter of 50 to 300 nm can be captured (Fig. 4A–C). The measured cutoff size was in good agreement with the theoretical calculation of the inertial impactor

(~70 nm) (Fig. 4F). The minimal collection efficiency at 3 L/min is above 20% rather than zero likely due to some airflow penetration, which is consistent with the collection performance of porous materials reported previously (51, 52). The curvatures on the impactation surface induced by round jets also increased the jet-to-plate distance/nozzle size (S/W) ratio, to affect the cutoff diameter (53). Nonetheless, the roughness of the surface increases the slip length for flows up to the micron level (54), which is the Navier slip condition, to increase the capture probability of particles.

Aerosol-into-Liquid Collection and Detection of Particle-Bound Pb(II)

The mean mobility diameter of the lab-generated aerosol (including Pb(II) and PM₁₀-like aerosol) was 37.41 ± 6.12 nm (Fig. 5A), whereas that of the ambient aerosol in Dübendorf, Switzerland, during the experiment was 117.98 ± 3.51 nm (SI Appendix, Fig. S9). The particle number of PM_{0.5}, PM_{0.5-1}, PM_{1-2.5}, and PM_{2.5-10} of the Pb(II) aerosols accounted for 97.4%, 2.1%, 0.5%, and 0.1% in terms of particle number, respectively (Fig. 5B). The ambient aerosol in Dübendorf during the experiment has a larger mean mobility diameter, with PM_{0.5}, PM_{0.5-1}, PM_{1-2.5}, and PM_{2.5-10} number fraction of 90.8%, 7.6%, 1.4%, and 0.2%, respectively. In contrast, PM₁₀-like aerosol can be representative of real-world aerosol with an increased number of particles larger than 1 μm [e.g., dust-enriched aerosol and fire-induced aerosol (55)], which consists of 71.8%, 22.6%, 5.5%, 0.1% of PM_{0.5}, PM_{0.5-1}, PM_{1-2.5}, and PM_{2.5-10}, respectively (Fig. 5B). PM₁₀-like particles were collected from the road tunnel “Wisostrada” in Warsaw, Poland, with total carbon (11.1%) and Silicon (22.9%) as the major components (SI Appendix, Table S3), which were used to be re-aerosolized in the lab. In addition, the particle number of the lab-generated PM₁₀-like aerosol was up to 6.58 folds and 547.22 folds higher than that in the ambient

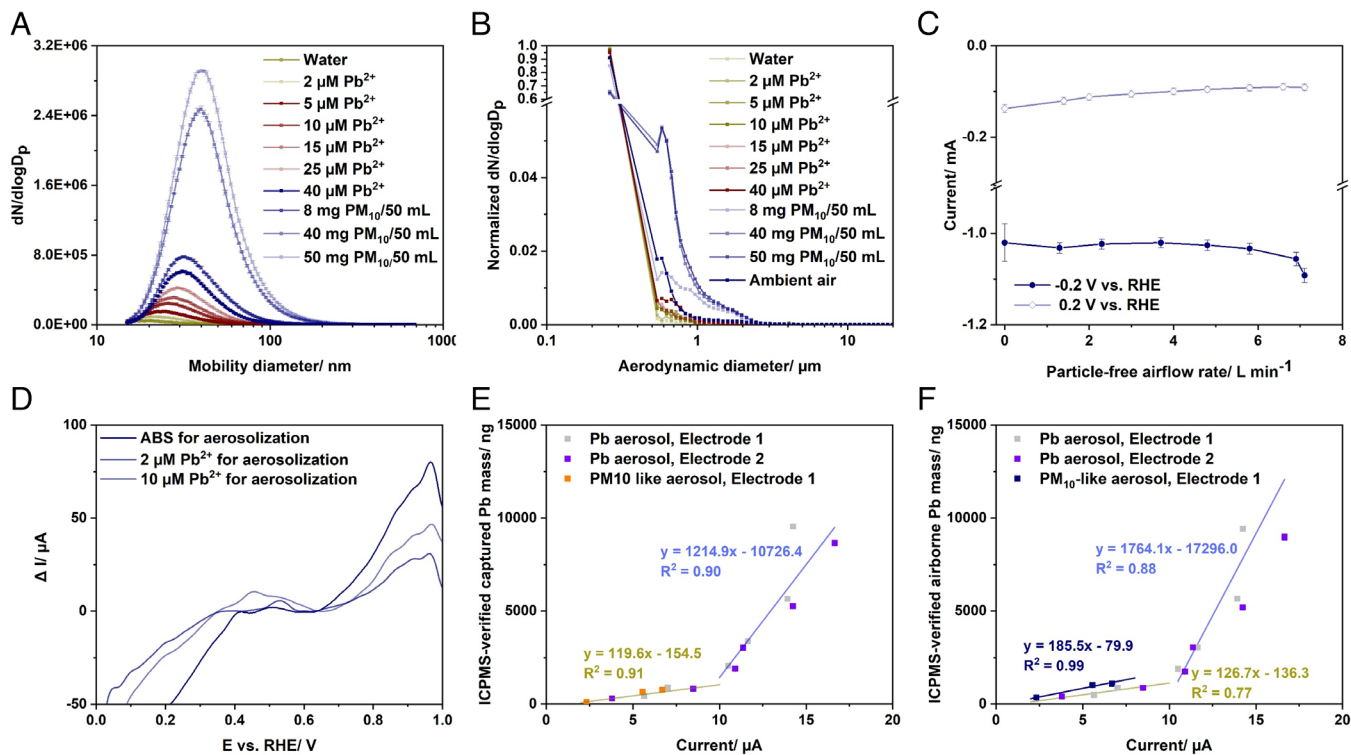


Fig. 5. Sensing performance using the lab-generated metal aerosol and PM₁₀-like aerosol. (A) SMPS scanning of the particle size distribution of the lab-generated Pb(II) particles and PM₁₀-like aerosol, (B) normalized particle size distribution of the lab-generated lead particles and PM₁₀-like aerosol in terms of aerodynamic diameter, (C) chronoamperometry current at 0.2 V and -0.2 V vs. RHE for about 1 min at different airflow rates, (D) example of SWV voltammetry of lab-generated Pb(II) aerosol, (E) concentration-dependent responses of the SWASV technique corresponding to captured Pb(II) into the aqueous phase from Pb(II) and PM₁₀-like aerosols, (F) concentration-dependent responses to airborne Pb(II) and PM₁₀-like aerosol using the SWASV technique. The relationships between current peaks and ICP-MS-verified concentrations using Pb aerosols were considered as the calibration curves. ICP-MS-verified concentrations were obtained from parallel filters and electrolytes followed by ICP-MS analysis.

environment according to the Aerodynamic Particle Sizer (APS) and SMPS measurements, respectively (*SI Appendix, Fig. S9*), which is also a typical characteristic of abrupt air pollution accidents. We also exploited the performance of the IAE system in the ambient environment. The result showed no Pb signal, which means the airborne Pb(II) concentration was below the limit of detection of the system (*SI Appendix, Fig. S10*). The parallel upstream and downstream filters determined by ICP-MS confirmed that no detectable Pb(II) was found during the same time duration of particle collection with a sampling flow rate of 4 L/min (*SI Appendix, Fig. S16 and Table S2*), which suggested that the common filter method followed by ICP-MS was also not able to detect the low level of atmospheric soluble metals with a 1-h collection time. A previous study also found a very low airborne Pb concentration of PM₁₀ in Dübendorf, Switzerland (0.344 ng/m³) (56). The metal compositions of the ambient environment mainly included Mg, Al, K, Ca, Fe, and Zn (56), which highlighted the absence of false positives using the IAE system in the ambient environment with the presence of low Pb(II) concentrations.

It was found that the particle-free airflow and pressure drop had a limited effect on hydrogen evolution (-1.04 ± 0.02 mA) and oxygen reduction (-0.10 ± 0.02 mA) at -0.2 V and 0.2 V, respectively (*SI Appendix, Fig. S11B*), indicating a relatively steady state of electrochemical environment under impingement of various flow rates up to 7.1 L/min. Compared to the cyclic voltammetry (CV) in the liquid phase, a higher current of oxygen reduction reaction at <0.25 V in the integrated system indicated the strong exposure of the membrane electrode to oxygen in the air (*SI Appendix, Fig. S11D*). In particular, the deposition current at 0 V was -1.34 ± 0.26 mA at equilibrium with the AILE

electrode in the IAE system, which was 5.25 folds higher than that completely in the liquid phase. The oxygen reduction reaction might affect the Pb(II) deposition by occupying the limited electrochemical active sites. Nonetheless, the deposition current remained stable at -0.2 V and 0.2 V, where hydrogen evolution and oxygen reduction reaction dominated, respectively (Fig. 5C). It demonstrated that the airflow rate had a negligible effect on the AILE electrode in the IAE system, resulting in a steady electrochemical environment for Pb(II) sensing.

The current peaks were mainly in the range of 0.3 to 0.6 V and increased with higher airborne Pb(II) concentration (Fig. 5D). It showed a linear relationship between peak currents and Pb(II) concentrations (Fig. 5E and F). The limit of detection of the membrane electrode was 90.3 ng with a 1-h collection duration, according to the equation $LOD = 3\delta/S$, where δ is the SD of the background current signal and S is the ratio of the current signal to the captured Pb mass (ng). The electrolyte volume contained in the integrated system was around 43 mL after a 1-h operation, so the limit of detection was 10.1 nM, which was 7.8 folds lower than that of the detection in the liquid phase. The sensing conditions of the conventional aqueous detection and aerosol-into-liquid concept were listed in *SI Appendix, Table S4*. It demonstrated the sensing concept of air-into-liquid increased the mass transport of Pb(II) by constantly introducing Pb(II) through a shorter distance (i.e., the thickness of the AILE electrode) than the diffusion layer in the conventional aqueous detection. The detection ratio of PM₁₀-like aerosols was $90.2 \pm 17.1\%$, indicating a minimum effect from insoluble particles based on the aerosol-into-liquid transfer and selectivity of the AILE electrode. The detection ratio was the calculated Pb mass obtained from electrochemical signals according

to the calibration curves (Pb aerosols in Fig. 5E) compared to ICP-MS-verified concentrations. Again, the high detection ratio of PM₁₀-like aerosols highlighted the system selectivity in the presence of real-world samples. For example, the concentrations of total carbon, calcium, chlorine, and iron in PM₁₀-like aerosols were over 985.2, 557.9, 88.8, and 337.6 folds higher than that of Pb, respectively (SI Appendix, Table S3). The penetration ratio of the Pb(II) aerosol and PM₁₀-like aerosol through the membrane electrode was 99.4 ± 2.2% and 62.1 ± 22.5%, respectively. The lower penetration of PM₁₀-like aerosol is likely due to the particle loss around nozzles and penetration loss through insoluble particle loads. The penetration of soluble metals could be a preprocessing-free process (e.g., without sonication), and a previous study indicated that it could cause relatively lower recoveries of Pb (87.0%) and Cu (78.2%), in comparison with recoveries of Pb (91.6%) and Cu (87.3%) after sonication (57). The limit of detection for airborne Pb aerosol and PM₁₀-like aerosol in the environment was 95.7 ng and 140.0 ng with 1-h collection at 7.1 L/min, respectively. This limit of detection might be applied in heavily polluted regions [e.g., Hanoi (58), Beijing (59), and Xi'an (60) with a soluble Pb concentration of around 100 ng/m³ and abrupt air pollution events [e.g., wildfire (61) and festival fireworks (62) with an elevated Pb concentration of above 100 ng/m³]. It was noted that a huge potential to improve the limit of detection was discussed in the discussion section below. The collection efficiency of lab-generated Pb and PM₁₀-like aerosols in the integrated system was 84.7 ± 3.3%. Overall, the integrated system exhibited the applicability, selectivity, and stability of our IAE system for the Pb(II) collection and detection in the aerosol with high particle numbers and large particle sizes, which usually appears in abrupt air pollution accidents.

Mechanism of Aerosol-into-Liquid Collection and Sensing. The flow velocity field within the system showed that the flow rate was generally lower than 3 m/s, whereas it increased up to 160 m/s around the nozzle plate (Fig. 6A). Both experimental and simulation results showed that the jet-to-electrode distances affected the collection efficiency (Fig. 6B). Simulation analysis indicated that the aerosol-into-liquid concept could achieve a faster mass transport with a longer collection time, compared to the conventional aqueous detection (Fig. 6C). For example, the mass transport using the aerosol-into-liquid concept would increase up to 15-fold of that using the conventional aqueous detection with a collection time of 5 min. For the aerosol-into-liquid concept, the mass transport of metal ions reaching the electrode surface was mainly driven by the concentration gradient, while the electrolyte evaporation in the opposite direction of metal diffusion, and metal adsorption had a minor effect on the mass transport (SI Appendix, Fig. S20C). Nonetheless, the sufficient mass transport in the aerosol-into-liquid concept was not fully utilized in the Pb(II) sensing, and the utilization ratio was 4.65 ± 1.02% compared to the conventional aqueous detection (SI Appendix, Fig. S12), which was likely due to the stronger oxygen reduction reaction on the electrode surface in the aerosol-into-liquid concept (SI Appendix, Fig. S11D). Since the detection of Pb(II) was an accumulation of reduced Pb on the electrode surface, the utilization ratio was defined as the fraction of reduced Pb(II) reaching the electrode surface. Fig. 6D indicated that the air jet with a velocity of 100 m/s impinging on the electrolyte-supported membrane led to vertical deformation, which had a minor effect on the collection performance according to the

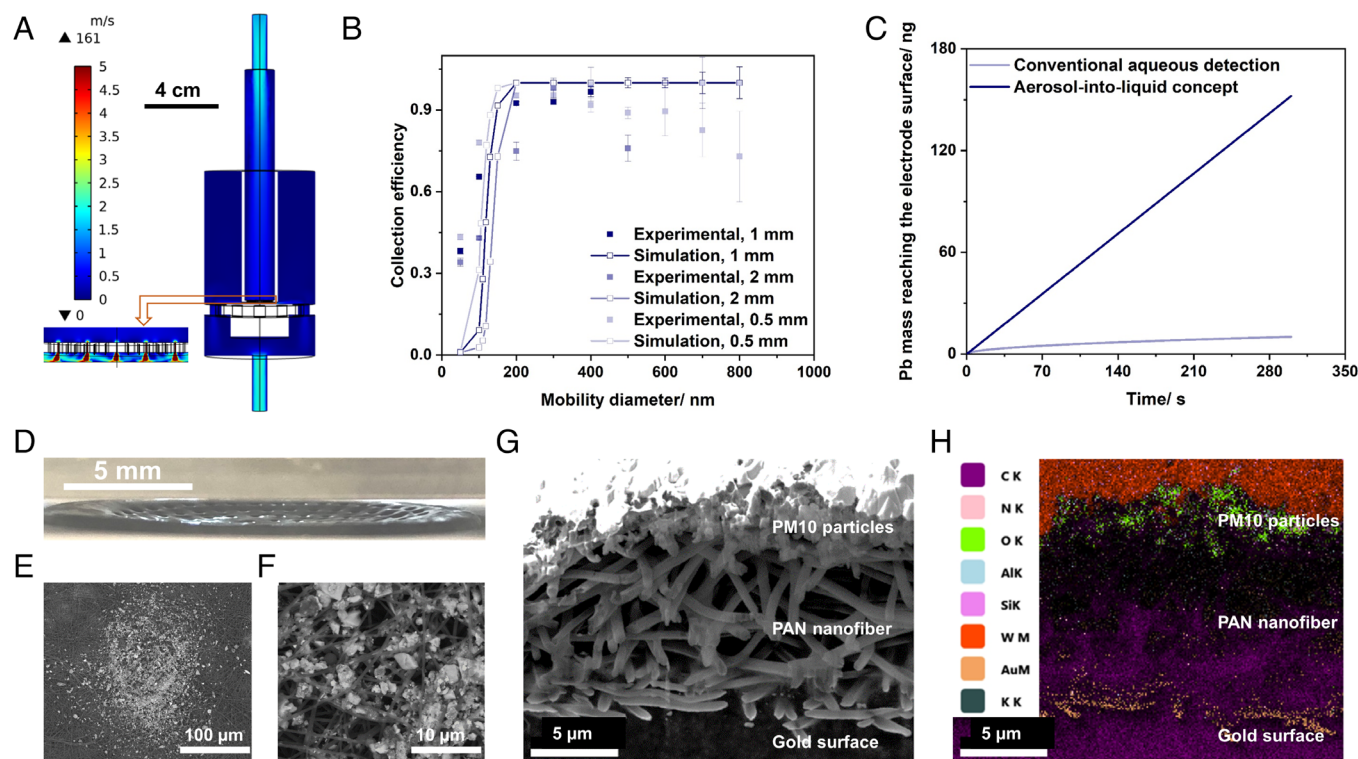


Fig. 6. Collection and sensing mechanism using the IAE system. (A) Airflow field inside the IAE system at an inflow rate of 7.1 L/min, (B) comparison of experimental and simulated collection efficiency with 151 × 0.1 mm (diameter) nozzles at 7.1 L/min in terms of jet-to-plate distance, (C) Diffusion simulation of Pb(II) based on the concept of aerosol-into-liquid collection and detection, and the conventional detection method, given a Pb(II) concentration of 205 nM, (D) photo of electrolyte-supported electrode membrane deformation with the flow jet at 100 m/s through 151 × 0.1 mm nozzles, (E and F) SEM image of the particle collection on the AILE electrode, (G) cross-sectional plasma FIB/SEM image of the AILE electrode with collected particles, (H) cross-sectional elemental mapping of the AILE electrode with collected particles.

good agreement between experimental and simulation results shown in Fig. 6B.

SEM images showed that PM₁₀ particles were well-distributed homogeneously among nanofibers of the membrane surface (Fig. 6E and F), rather than forming deposition build-ups. The diameter of the particle distribution area facing each nozzle was around 200 μm (Fig. 6E). PM₁₀ particles were mostly collected on the nanofiber surface (Fig. 6G and H), which provides a unique way to avoid fouling from solid particles on the downward electrode surface resulting in the disabled electrode. In contrast, the soluble fraction penetrates and reaches the electrode surface for electrochemical sensing, as shown in SEM mapping that Na and K were also determined in the middle of the AILE electrode cross-section (*SI Appendix, Fig. S13*). Therefore, the electrolyte-supported PAN membrane electrode demonstrated a stable and efficient structure for particle collection and immediate metal detection by separating gas and liquid phase via a solid nanofiber membrane. Metals could be rapidly released for particles immediately after contacting the aqueous solution (63). Capillary forces are dominant in attaching particles at the air–water interface (64), and the presence of acetic acid in some cases enhances the hydrophilic properties of particles (65). These factors could facilitate the metal dissolution and mass transport through the electrode. The aerosol-into-liquid collection of hydrophilic malachite green particles indicated sufficient aerosol-into-liquid dissolution and transfer of soluble particles through the membrane electrode, resulting in a relatively homogeneous distribution of malachite green on the membrane and the electrolyte, respectively (*SI Appendix, Fig. S14*). It also indicated that based on the concept of aerosol-into-liquid collection and detection achieved via the AILE electrode, sample preprocessing was not necessarily applied using the IAE system for collection and detection. It was noted that the aerosol-into-liquid dissolution of soluble particles could be distinct from that of insoluble particles in aerosol (e.g., longer penetration distance due to particle loads, less dissolution efficiency from insoluble-containing particles).

Discussion

A concept of aerosol-into-liquid capture and detection was introduced to design the on-site, near-continuous, low-cost, and miniaturized system for capturing and determining airborne soluble metals. This concept opens up a new way for sampling and measurement, which can rapidly respond to atmospheric processes and pollution events. The IAE system designed based on this concept was validated using lab-generated and ambient aerosols. The electrochemical detection was achieved under a high airflow rate (e.g., 100 m/s) and low pressure (e.g., 0.85 atm). Interestingly, the collection and detection performances were superior compared to conventional collection techniques (e.g., metal-based impactors) and electrochemical detection methods (e.g., electrochemical detection in solutions with a homogenous concentration), such as lower cutoff sizes, minimum particle bouncing, minimum sample preprocessing, a lower limit of detection, and minimum insoluble particle fouling. It was suggested that future designs based on this concept should benefit not only from reduced system sizes but also from improved collection and detection performance. The electrochemical voltammetry methods can achieve the detection of multiple metals such as Cd, Pb, Cu, Fe, and Ni ions (66), which are expected to be realized in our system via modifying either sensing materials or sensing techniques. As shown in *SI Appendix, Table S1*, the electrochemical method has been successfully developed to detect multiple metals such as Fe, Cu, Ni, Zn, and Pb ions in aerosol samples on the same electrode without significant interference from unintended metals. These studies show the limit of detection of

different metals was comparable to that of Pb(II) obtained in this work, which indicates that a similar limit of detection could be achieved for other airborne metals. Membranes should be carefully selected and developed depending on the types of metals to be sampled and detected, to avoid significant adsorption or changes in the chemical form of soluble metals. In the future, we also anticipate that the system offers a platform for collecting and detecting other soluble components in the aerosol. Moreover, the availability and development of the AILE electrode by designing pore size, thickness, and structure of nanofibers could also enable the collection and detection of aerosol insoluble components.

For the collection scheme, it is noted that the aerosol-into-liquid concept is different from the particle-into-liquid sampler (PILS), which employs particle condensation growth to capture particles into liquid (67). In contrast, the collection method of this work is similar to a wet-surface impactor, where the liquid impaction film tends to collapse with a cutoff collection size of smaller than 200 nm due to the increased force of air jets (29). In comparison, the electrolyte-supported AILE electrode is capable of withstanding the air jets resulting in a cutoff size down to 50 nm. To avoid the sampling (e.g., PILS) and detection (e.g., UV-visible spectrophotometry (UV/VIS) spectrometer) units in sequence, the AILE electrode achieves the direct detection of soluble metals on one side after collecting particles on the other side. The separation of soluble fractions from total metals is a necessary step before determining metal solubility or bioaccessibility and exploring their relationship with adverse health effects such as reactive oxygen species (21). The conventional separation step involves sonication and submicrometer-graded filter filtration (68). In contrast, our concept and system are able to skip this step via the aerosol-into-liquid process.

To our knowledge, there are several commercial continuous metal monitors such as Xact 625i and PX-375, to achieve a low limit of detection with a high time resolution (*SI Appendix, Table S5*). However, our concept and IAE system could fit in the field where the shortages of these commercial instruments are. For instance, the IAE system based on the aerosol-into-liquid concept can be adapted into decentralized and rapid monitoring at a high spatial resolution because of up to 40X smaller size and 400X lower cost as shown in *SI Appendix, Table S5*. Screen-printed electrodes enable low-cost, miniaturized systems for decentralized and on-site determination of airborne metals (69). Our system functions similarly to the combination of a screen-printed electrode system and a sampling method of airborne metals, which also suggests that our proposed system can be further miniaturized and simplified if a screen-printed porous and hydrophilic working electrode is available to replace the three electrodes used in the present system. More importantly, the IAE system is sensitive to metal solubility, which is strongly associated with adverse health issues, whereas the available commercial instruments offer information on total elements. Overall, the aerosol-into-liquid concept will contribute to extensive measurements, understanding, and risk assessments of atmospheric soluble metals.

The range of soluble fractions of metals in PM varies greatly depending on many factors such as sampling locations and emission sources. For example, a review summarized the soluble metals in PM using water as the leaching agent, and the soluble fraction of Pb was in a wide range of 3.8 to 88% (20). There are many leaching agents used for the extraction of bioaccessible metals, such as water, acetate buffer, artificial lysosomal fluid, and Gamble's solution, which exhibit various levels of metal solubility and might bring about different definitions of bioaccessible metals (20). The electrolyte (0.1 M acetate buffer) we used in the experiment could be relevant in assessments of bioaccessibility and investigations of

metal toxicity, however, the results might differ from the metal dissolution in vivo. Further, the electrolyte in the proposed system can be changed for the dissolution of airborne metals according to the needs of target applications (e.g., simulation of airborne metal dissolution in body fluids). The extraction of soluble metals in this work was performed in 45 mL of 0.1 M acetate buffer (pH 4.45) for 1 h at room temperature. Further investigations based on the proposed concept and system could also be devoted to the variability of soluble metals by separating insoluble and soluble metals using the Janus-membrane electrode, which might effectively contribute to the understanding of soluble metals.

Despite the excellent performance validated using re-aerosolized PM₁₀-like particles (real-world samples), the monitoring of soluble metals using the system in ambient air is still challenging due to the higher limit of detection compared to ambient Pb concentrations in most cases. Nonetheless, based on this concept, the limit of detection is expected to achieve potential improvements by advancing the used electrochemical voltammetry method. For example, as the collection time of 1 h is carried out using the system, the limit of detection in a unit of ng/m³ is possibly reduced by prolonging the collection time to collect more air volume (e.g., by 2X with a 2-h collection time). Only 4.65% Pb mass is utilized in the Pb(II) sensing compared to the conventional aqueous detection likely due to the strong oxygen reduction reaction, the limit of detection therefore could be potentially improved (by 20X if Pb mass is fully utilized) using oxygen scavenger agents in the electrolyte. Moreover, a bare gold electrode is used to prove the aerosol-in-to-liquid concept in this work, which can be modified by adding nanostructures or changing material compositions to further improve the limit of detection ideally by order of magnitudes.

Methods

Chemicals and Reagents. Deionized water (>18.2 MΩ cm) was derived from the Milli-Q system (Merck Millipore). Polyacrylonitrile (PAN, Mw 534000, powder), N, N-dimethylformamide (DMF, ≥ 99.8%), lead (II) nitrate (99.999%), glacial acetic acid (99.7%), sulfuric acid (95 to 98%), potassium hydroxide (>85%), and cadmium nitrate tetrahydrate (99.997%) were purchased from Sigma-Aldrich. Copper (II) nitrate hemi(pentahydrate) (98%) was obtained from Alfa Aesar. In addition, 0.1 mM metal ions solutions were prepared for further dilution in 0.1 M acetate buffer (pH 4.45).

Preparation of the AILE Electrodes. The commonly used materials for sensing transition-metal ions in terms of electrochemical sensors are glassy carbon, gold, and boron-doped diamond, besides mercury and bismuth (70). Here, we employed a PAN nanofiber membrane and gold as aerodynamic functional material and electrochemical sensing surface, respectively. The PAN nanofiber membrane with a thickness of ~30 μm was obtained by electrospinning (43). In brief, 8 wt.% PAN/DMF solution was prepared and employed for 2 h with an extrusion rate of 1 mL/h, and the distance between the tip and collector was 15 cm. Prior to gold deposition, the PAN nanofiber membrane was laminated at 75 °C (GBC Fusion 1100 L), to improve lamination and mechanical strength (43). Gold (~50 nm) was sputtered on one side of the PAN nanofiber membrane by magnetron sputtering (Leica EM ACE 600).

Due to the adsorption of metal ions onto PAN nanofiber (71, 72), 40 mg of prepared PAN nanofiber membrane (~135 cm²) was put into 30 mL of a 10 μM Pb solution for 24 h and then into the Pb-free 0.1 M acetate buffer and then MilliQ water for 24 h after rinsing with MilliQ water, respectively, to examine the adsorption and desorption behaviors. The sample solution was shaken on a rotary shaker (KS 260 basic, IKA), operating at room temperature and 100 rpm. Then, 1 mL of the sample solution was withdrawn at 10 min, 30 min, 1 h, 2 h, 5 h, 10 h, and 24 h, which was acidified to 1% (w/w) HNO₃ and refrigerated until the ICP-MS measurement. The PAN nanofiber was then transferred into 30 mL 10 μM Pb solution for 24 h again to investigate the repeated adsorption behavior. The electrolyte uptake ratio of the PAN nanofiber-based gold electrode was approximately 50/g. The fiber diameter and porosity of the PAN nanofiber membrane

and PAN nanofiber-based gold electrode were determined with ImageJ 1.50e on SEM images. The gold wire (99.9%, MaTeck) was used to connect the potentiostat with PAN nanofiber-based gold electrode. The Teflon tape was used to fix the working area of PAN nanofiber-based gold electrodes (Ø = 1.6 cm) for the detection of metal ions in the liquid phase (SI Appendix, Fig. S1). Cyclic voltammetry is in the potential range of -0.2 to 1.2 V vs. Reversible hydrogen electrode (RHE) for about 20 cycles and chronoamperometry at 1.0 V was performed to activate the PAN nanofiber-based gold electrode in 0.1 M acetate buffer (pH 4.45) and electrochemically remove any impurities before the metal ions detection each time, to obtain the active and reproducible electrode surface (73).

Electrochemical Detection Methods in the Liquid Phase. The electrochemical studies were carried out using either SP-240 potentiostat or SP-300 potentiostat (Bio-Logic Science Instruments). Specifically, the detection of metal ions in the liquid phase was conducted in a standard three-electrode electrochemical cell (saturated with Argon during experiments) with an Ag/AgCl (SI Analytics or Microelectrodes, 3 M KCl) reference electrode (SI Appendix, Fig. S15) and Pt wire counter electrode. Then, 100 mL of 0.1 M acetate buffer (pH 4.45), prepared by mixing glacial acetic acid and potassium hydroxide, was the electrolyte to eliminate sample matrix effects. A gold rotating disk electrode (RDE) (A_{geo} = 0.20 cm²) was sonicated in 0.15 M nitrate acid and 0.2 M hydrochloric acid for 10 min, respectively, and then polished with 0.05 μm alumina polishing slurry (Pace Technologies). The rotation rate (1,600 rpm) of gold RDE was controlled by Pine instruments set up for RDE.

The working principle is accumulating soluble metals on the electrode surface (metal reduction) and then obtaining the signal (metal oxidation). Anodic stripping voltammetry (ASV) is the technique that allows metal reduction and then metal oxidation. The following parameters were used: conditioning potential (E_{cond}) 1 V vs. RHE for 4 min, deposition potential (E_{dep}) -0.2 V for 5 min, and equilibration time (t_{eq}) for 30 s (only in the case of RDE). The stripping charge using ASV was calculated by integrating current over time, and then, background charging should be subtracted from it. Square wave anodic stripping voltammetry (SWASV) is widely used in the detection without oxygen removal (74). The following parameters were used: conditioning potential (E_{cond}) 1 V vs. RHE for 4 min, deposition potential (E_{dep}) -0.2 V for 5 min, Square Wave (SW) amplitude (E_{amp}) 25 mV, step potential (E_{step}) 5 mV, pulse width 5 ms. Experiments with each concentration were repeated three times, to obtain the deviation and ensure accuracy.

The IAE System for Detecting Aerosol Pb(II). Materials (e.g., metal, glass, and PTFE) for the electrochemical sensing system should be carefully selected. For example, stainless steel was used for the tubing and nozzle plate to avoid particle deposition and losses during the particle collection, whereas PTFE was employed in the electrochemical cell due to its hydrophobicity, conductive resistance, and contamination resistance. From the perspective of electrochemistry, a small volume of the cell (Ø = 1.6 cm) was employed to reduce mass transport and improve the detection limit. PAN nanofiber-based gold electrode (3 × 3 cm) with a gold wire was mounted on PTFE plates, to achieve a precise distance between the jet and the electrode via a nozzle-to-plate distance adjuster. The actual collection and sensing area (Ø = 1.6 cm) was isolated by a circle of glue (Araldite, Switzerland) to achieve waterproof beyond the real sensing area (SI Appendix, Fig. S1). The PAN side without gold was used to face flows and capture particles. It should be noted that the PAN side with a gold surface immerses into the electrolyte, to alleviate the intense reaction of oxygen reduction on active sites during the metal deposition. The counter and flexible reference electrode was long enough to reach the PTFE plate part so that the distance between the working and reference or counter electrode was minimized to reduce the ohmic drop induced by the electrolyte.

For the aerodynamic part, a microorifice cascade impactor was designed and fabricated using stainless steel for particle collection based on inertial impaction. The flow rate should be increased gradually to avoid the sudden spilling of the electrolyte from the PTFE cell. The Stokes number (Stk) was calculated based on the following equation.

$$\text{Stk} = \frac{\rho_p d_p^2 C_c U}{9\mu W}$$

where ρ_p is the particle density, d_p is the 50% cutoff diameter of particles, C_c is the slip correction factor, U is the average jet velocity, μ is the dynamic viscosity

of the air ($1.8 \times 10^{-5} \text{ kg ms}^{-1}$), and W is the diameter of the nozzle. The Stokes number (Stk_{50}) should be 0.49 using a round-nozzle impactor (75). The cutoff size diameter is calculated with the following equation:

$$D_{p50} = \sqrt{\frac{9\pi\mu D_j^3 Stk_{50}}{4\rho_p Q C_c}}$$

where D_j is the diameter of the nozzle and Q is the flow rate. Meanwhile, Reynolds number (Re) should be in the range of 500 to 3,000 to achieve maximum collection efficiency, which is defined as follows.

$$Re = \frac{\rho W V_0}{\mu}$$

where ρ is the gas density, W is the nozzle diameter, V_0 is the velocity, and μ is the viscosity. To achieve a relatively low Reynolds number and pressure drop, we chose 151 and 201 nozzles. Considering the low porosity (1%) of the nozzle plate to avoid the cross-flow effect, the diameter of the tube is set to 16 mm. Impactor operating parameters such as S/W should be in the range from 0.5 to 10 (29, 76). Considering S/W for the eighth stage in MOUDI (77), the jet-to-plate distance was set to 1 mm. The aerodynamic and electrochemical function modules were connected through two PTFE tubing, to balance air pressure and electrolyte height.

Evaluation of Collection Efficiency and Sensing Performance of the IAE System. A homemade atomizer and a diffusion dryer were used to generate and dry the aerosol with a flow rate of 3.8 L/min. Size resolved information including size distribution and particle number was measured using the scanning mobility particle sizer (SMPS), which consists of a differential mobility analyzer (DMA, TSI model 3081) and a condensation particle counter (TSI model 3775). The concentration of metal ions in the aerosol was determined by ICP-MS. The particle number and concentration of aerosol were determined by measuring upstream (C_{up}) and downstream (C_{down}). The collection efficiency (η) of the inertial impactor was calculated as follows:

$$\eta = \frac{C_{up} - C_{down}}{C_{up}} \times 100\%$$

The particle loss and aerosol-into-liquid transfer efficiency of the system were evaluated using NaCl monodisperse particles selected by DMA and collected for 2 h. More specifically, the nozzle plate, PAN membrane, and PTFE plate were eluted by 10 mL milli-Q water after particle collection, and 10 mL electrolyte (here, we used Milli-Q water to avoid Na contamination) in the system was also preserved for NaCl determination by ICP-MS. NaCl concentrations from the PAN membrane and electrolyte were used to estimate the aerosol-into-liquid transfer efficiency. To simulate and visualize the collection of trace airborne soluble elements in the integrated system, 0.2 wt% malachite green solution was used in the particle generation system to produce colored particles for 1 h.

To correlate the concentration of metal ions in the aerosol with the electrochemical signal, two filter holders with 1 μm 47 mm polycarbonate membrane filters (effective diameter 35 mm) (Sterlitech) or 0.45 μm cellulose nitrate filters

(Sartorius Stedim biotech) were placed in the effluent flow of the electrochemical sensing system and in parallel at the same flowrate (i.e., 7.1 L/min), respectively (SI Appendix, Figs. S16 and S17). The filters were ultrasonically extracted for 30 min in centrifuge tubes using 1 mL acetate buffer. Subsequently, 9 mL water was added and combined ultrasonically for another 30 min. The combined extracts were filtered using syringe filters (0.2 μm) to remove the insoluble fractions.

Pb(NO₃)₂ and PM10-like (trace elements) ERM® Certified Reference Material (European Reference Materials, ERM-CZ120) in acetate buffer (pH 4.45) were generated from a homemade atomizer as particles and used for establishing the calibration curve. Then, 50 mg PM₁₀-like (trace elements) ERM® Certified Reference Material, was suspended in 50 mL acetate buffer (pH 4.45) and shaken on a vortex shaker (uniTEXER, LLG Labware) at 1,000 rpm for 5 min, followed by sonication for 30 min (78). PM10 suspension solution was diluted using acetate buffer to obtain different aerosol concentrations. It is noted that the Pb solution and PM suspension were prepared with acetate buffer to reduce metal hydration. The collection time of the integrated system was 1 h. Ambient aerosol around the laboratory ($n = 2$) was measured for the performance evaluation in the real-world environment. The following parameters for the electrochemical technique were used: conditioning potential (E_{cond}) 1 V vs. RHE for 4 min, deposition potential (E_{dep}) 0 V for 1 h, SW amplitude (E_{amp}) 25 mV, step potential (E_{step}) 5 mV, pulse width 5 ms, and quiet time (no airflow) 0 min.

Numerical Simulation of the Aerosol Dynamics and Metal Ion Diffusion.

The aerosol dynamics and particle capture were simulated using COMSOL Multiphysics 6.0. Laminar flow and particle tracing for fluid flow modules were involved. The geometric dimensions were set the same as the real setup and further simplified. In the aerodynamic simulation, the Reynolds number was smaller than 1,000, and therefore, the laminar regime could be assumed (79). Matlab was used to simulate the Pb(II) diffusion processes in the case of conventional aqueous detection and the aerosol-into-liquid concept. The AILE electrode was simplified into a film with a thickness of 15 μm due to the complex structure of nanofibers on a millimeter scale. A detailed description of the simulations can be found in the SI Appendix.

Data, Materials, and Software Availability. All study data are included in the article and/or SI Appendix.

ACKNOWLEDGMENTS. Y.-B.Z. and F.J. acknowledge the financial support from the China Scholarship Council. T.C. and C.L. acknowledge the Swiss National Science Foundation for the financial support (project 184817). Y.-B.Z. thanks Daniel Rechenmacher for the drawing and manufacture of the aerodynamic/electrochemical sensing system. We gratefully acknowledge ScopeM at ETH Zürich, especially Karsten Kunze, for their support and assistance in this work.

Author affiliations: ^aInstitute of Environmental Engineering, ETH Zürich, Zürich 8093, Switzerland; ^bLaboratory for Advanced Analytical Technologies, Empa, Swiss Federal Laboratories for Materials Science and Technology, Dübendorf 8600, Switzerland; ^cEnvironmental Engineering Institute, School of Architecture, Civil and Environmental Engineering, École Polytechnique Fédérale de Lausanne, Lausanne 1015, Switzerland; ^dBioenergy and Catalysis Laboratory, Energy and Environment Research Division, Paul Scherrer Institut, Villigen 5232, Switzerland; ^eFilter Test Center, College of Resources and Civil Engineering, Northeastern University, Shenyang, Liaoning 110819, China; and ^fDepartment of Inorganic and Analytical Chemistry, University of Geneva, Geneva 1211, Switzerland

1. Y. Chang *et al.*, First long-term and near real-time measurement of trace elements in China's urban atmosphere: Temporal variability, source apportionment and precipitation effect. *Atmos. Chem. Phys.* **18**, 11793–11812 (2018).
2. H. Li, X. Qian, Q. G. Wang, Heavy metals in atmospheric particulate matter: A comprehensive understanding is needed for monitoring and risk mitigation. *Environ. Sci. Technol.* **47**, 13210–13211 (2013).
3. J. Duan, J. Tan, Atmospheric heavy metals and arsenic in China: Situation, sources and control policies. *Atmos. Environ.* **74**, 93–101 (2013).
4. N. M. Mahowald *et al.*, Aerosol trace metal leaching and impacts on marine microorganisms. *Nat. Commun.* **9**, 2614 (2018).
5. G. Aragay, A. Merkoçi, Nanomaterials application in electrochemical detection of heavy metals. *Electrochim. Acta* **84**, 49–61 (2012).
6. H. Z. Tian *et al.*, Quantitative assessment of atmospheric emissions of toxic heavy metals from anthropogenic sources in China: Historical trend, spatial distribution, uncertainties, and control policies. *Atmos. Chem. Phys.* **15**, 10127–10147 (2015).
7. G. Le Roux *et al.*, Learning from the past: Fires, architecture, and environmental lead emissions. *Environ. Sci. Technol.* **53**, 8482–8484 (2019).
8. K. E. Smith, D. Weis, C. Chauvel, S. Moulin, Honey maps the Pb fallout from the 2019 fire at Notre-Dame cathedral, Paris: A geochemical perspective. *Environ. Sci. Technol. Lett.* **7**, 753–759 (2020).
9. R. Levin *et al.*, The urban lead (Pb) burden in humans, animals and the natural environment. *Environ. Res.* **193**, 110377 (2021).
10. C. F. Isley, M. P. Taylor, Atmospheric remobilization of natural and anthropogenic contaminants during wildfires. *Environ. Pollut.* **267**, 115400 (2020).
11. I. Campos, N. Abrantes, J. J. Keizer, C. Vale, P. Pereira, Major and trace elements in soils and ashes of eucalypt and pine forest plantations in Portugal following a wildfire. *Sci. Total Environ.* **572**, 1363–1376 (2016).
12. J. Korsiak *et al.*, Long-term exposure to wildfires and cancer incidence in Canada: A population-based observational cohort study. *Lancet Planet Health* **6**, e400–e409 (2022).
13. V. Bollati *et al.*, Exposure to metal-rich particulate matter modifies the expression of candidate microRNAs in peripheral blood leukocytes. *Environ. Health Perspect.* **118**, 763–768 (2010).

14. Y. Zhang, X. Ji, T. Ku, G. Li, N. Sang, Heavy metals bound to fine particulate matter from northern China induce season-dependent health risks: A study based on myocardial toxicity. *Environ. Pollut.* **216**, 380–390 (2016).
15. E. Resongles *et al.*, Strong evidence for the continued contribution of lead deposited during the 20th century to the atmospheric environment in London of today. *Proc. Natl. Acad. Sci. U.S.A.* **118**, e2102791118 (2021).
16. T. Schwaba *et al.*, The impact of childhood lead exposure on adult personality: Evidence from the United States, Europe, and a large-scale natural experiment. *Proc. Natl. Acad. Sci. U.S.A.* **118**, e2020104118 (2021).
17. W. Birimi, A. G. Allen, F. Bary, R. M. Harrison, Trace metal concentrations and water solubility in size-fractionated atmospheric particles and influence of road traffic. *Environ. Sci. Technol.* **40**, 1144–1153 (2006).
18. W. Li *et al.*, Microscopic observation of metal-containing particles from chinese continental outflow observed from a non-industrial site. *Environ. Sci. Technol.* **47**, 9124–9131 (2013).
19. S. Canepari, M. L. Astolfi, S. Moretti, R. Curini, Comparison of extracting solutions for elemental fractionation in airborne particulate matter. *Talanta* **82**, 834–844 (2010).
20. A. Mukhtar, A. Limbeck, Recent developments in assessment of bio-accessible trace metal fractions in airborne particulate matter: A review. *Anal. Chim. Acta* **774**, 11–25 (2013).
21. Y. Lyu, H. Guo, T. Cheng, X. Li, Particle size distributions of oxidative potential of lung-deposited particles: Assessing contributions from quinones and water-soluble metals. *Environ. Sci. Technol.* **52**, 6592–6600 (2018).
22. M. Shiraiwa *et al.*, Aerosol health effects from molecular to global scales. *Environ. Sci. Technol.* **51**, 13545–13567 (2017).
23. D. Foppiano, M. Tarik, E. Müller Gubler, C. Ludwig, Emissions of secondary formed ZnO nano-objects from the combustion of impregnated wood. An online size-resolved elemental investigation. *Environ. Sci. Technol.* **52**, 895–903 (2018).
24. S. Giannoukos *et al.*, Real-time detection of aerosol metals using online extractive electrospray ionization mass spectrometry. *Anal. Chem.* **92**, 1316–1325 (2020).
25. P. Rai *et al.*, Characteristics and sources of hourly elements in PM10 and PM2.5 during wintertime in Beijing. *Environ. Pollut.* **278**, 116865 (2021).
26. J. M. Creamean *et al.*, Colorado air quality impacted by long-range-transported aerosol: A set of case studies during the 2015 Pacific Northwest fires. *Atmos. Chem. Phys.* **16**, 12329–12345 (2016).
27. D. Wang, M. H. Sowlat, M. M. Shafer, J. J. Schauer, C. Sioutas, Development and evaluation of a novel monitor for online measurement of iron, manganese, and chromium in ambient particulate matter (PM). *Sci. Total Environ.* **565**, 123–131 (2016).
28. D. Wang, M. M. Shafer, J. J. Schauer, C. Sioutas, A new technique for online measurement of total and water-soluble copper (Cu) in coarse particulate matter (PM). *Environ. Pollut.* **199**, 227–234 (2015).
29. A. Karlsson, K. Irgum, H.-C. Hansson, Single-stage flowing liquid film impactor for continuous on-line particle analysis. *J. Aerosol Sci.* **28**, 1539–1551 (1997).
30. L. Cui, J. Wu, H. Ju, Electrochemical sensing of heavy metal ions with inorganic, organic and bio-materials. *Biosens. Bioelectron.* **63**, 276–286 (2015).
31. G. Aragay, J. Pons, A. Merkoçi, Recent trends in macro-, micro-, and nanomaterial-based tools and strategies for heavy-metal detection. *Chem. Rev.* **111**, 3433–3458 (2011).
32. K. Kalcher, L. M. Moretto, "Environmental Analysis by Electrochemical Sensors and Biosensors: Applications" in Nanostructure Science and Technology (Springer, 2015), vol. 2.
33. Y. Lu *et al.*, A review of the identification and detection of heavy metal ions in the environment by voltammetry. *Talanta* **178**, 324–338 (2018).
34. D. Buzica *et al.*, Comparison of voltammetry and inductively coupled plasma-mass spectrometry for the determination of heavy metals in PM10 airborne particulate matter. *Atmos. Environ.* **40**, 4703–4710 (2006).
35. J. Mettakoonpitak, D. Miller-Lionberg, T. Reilly, J. Volckens, C. S. Henry, Low-cost reusable sensor for cobalt and nickel detection in aerosols using adsorptive cathodic square-wave stripping voltammetry. *J. Electroanal. Chem.* **805**, 75–82 (2017).
36. F. Rueda-Holgado, L. Calvo-Blázquez, F. Cereceda-Balic, E. Pinilla-Gil, A semiautomatic system for soluble lead and copper monitoring in atmospheric deposition by coupling of passive elemental fractionation sampling and voltammetric measurement on screen-printed gold electrodes. *Microchem. J.* **124**, 20–25 (2016).
37. M. Takeuchi, S. M. R. Ullah, P. K. Dasgupta, D. R. Collins, A. Williams, Continuous collection of soluble atmospheric particles with a wetted hydrophilic filter. *Anal. Chem.* **77**, 8031–8040 (2005).
38. S. J. Fuller, F. P. H. Wragg, J. Nutter, M. Kalberer, Comparison of on-line and off-line methods to quantify reactive oxygen species (ROS) in atmospheric aerosols. *Atmos. Environ.* **92**, 97–103 (2014).
39. J. Zhou *et al.*, Development, characterization and first deployment of an improved online reactive oxygen species analyzer. *Atmos. Meas. Tech.* **11**, 65–80 (2018).
40. E. Ito, T. Tamadate, Y. Inomata, T. Seto, Water-based particle size magnifier for wet sampling of aerosol particles. *Aerosol Sci. Technol.* **55**, 1239–1248 (2021), 10.1080/02786826.2021.1940828.
41. D. Wang, J. Jiang, J. Deng, Y. Li, J. Hao, A sampler for collecting fine particles into liquid suspensions. *Aerosol. Air Qual. Res.* **20**, 654–662 (2020), 10.4209/aaqr.2019.12.0616.
42. Y.-B. Zhao *et al.*, Integrated aerodynamic/electrochemical microsystem for collection and detection of nanogram-level airborne bioaccessible metals. *Sens. Actuators B Chem.* **351**, 130903 (2022).
43. F. Jiang *et al.*, Conformal Cu coating on electrospun nanofibers for 3D electro-conductive networks. *Adv. Electron. Mater.* **6**, 1900767 (2020).
44. M. D. Scanlon *et al.*, Characterization of nanoporous gold electrodes for bioelectrochemical applications. *Langmuir* **28**, 2251–2261 (2012).
45. M. Libansky *et al.*, Basic electrochemical properties of sputtered gold film electrodes. *Electrochim. Acta* **251**, 452–460 (2017).
46. M. Finšgar, K. Khanari, B. Petovar, Copper-film electrodes for Pb(II) trace analysis and a detailed electrochemical impedance spectroscopy study. *Microchem. J.* **147**, 863–871 (2019).
47. C. M. Quiroa-Montalván *et al.*, Ordered mesoporous carbon decorated with magnetite for the detection of heavy metals by square wave anodic stripping voltammetry. *J. Electrochem. Soc.* **164**, B304–B313 (2017).
48. C.-H. Lin, P.-H. Li, M. Yang, J.-J. Ye, X.-J. Huang, Metal replacement causing interference in stripping analysis of multiple heavy metal analytes: Kinetic study on Cd(II) and Cu(II) electroanalysis via experiment and simulation. *Anal. Chem.* **91**, 9978–9985 (2019).
49. C.-J. Tsai *et al.*, Novel active personal nanoparticle sampler for the exposure assessment of nanoparticles in workplaces. *Environ. Sci. Technol.* **46**, 4546–4552 (2012).
50. C. Misra, S. Kim, S. Shen, C. Sioutas, A high flow rate, very low pressure drop impactor for inertial separation of ultrafine from accumulation mode particles. *J. Aerosol Sci.* **33**, 735–752 (2002).
51. C.-H. Huang, C.-J. Tsai, T.-S. Shih, Particle collection efficiency of an inertial impactor with porous metal substrates. *J. Aerosol Sci.* **32**, 1035–1044 (2001).
52. M. Marjamäki, J. Keskinen, Effect of impaction plate roughness and porosity on collection efficiency. *J. Aerosol Sci.* **35**, 301–308 (2004).
53. S. Park *et al.*, Stabilization of liquid instabilities with ionized gas jets. *Nature* **592**, 49–53 (2021).
54. S. Jiménez Bolaños, B. Vernescu, Derivation of the navier slip and slip length for viscous flows over a rough boundary. *Phys. Fluids* **29**, 057103 (2017).
55. X. Yang, C. Zhao, Y. Yang, X. Yan, H. Fan, Statistical aerosol properties associated with fire events from 2002 to 2019 and a case analysis in 2019 over Australia. *Atmos. Chem. Phys.* **21**, 3833–3853 (2021).
56. Y. Yue *et al.*, Size-resolved endotoxin and oxidative potential of ambient particles in Beijing and Zürich. *Environ. Sci. Technol.* **52**, 6816–6824 (2018).
57. K. Ashley, R. N. Andrews, L. Cavazos, M. Demange, Ultrasonic extraction as a sample preparation technique for elemental analysis by atomic spectrometry. *J. Anal. At. Spectrom.* **16**, 1147–1153 (2001).
58. T. T. Hien *et al.*, Soluble trace metals associated with atmospheric fine particulate matter in the two most populous cities in Vietnam. *Atmos. Environ.* **15**, 100178 (2022).
59. Q. Wang *et al.*, Characteristics of size-fractionated atmospheric metals and water-soluble metals in two typical episodes in Beijing. *Atmos. Environ.* **119**, 294–303 (2015).
60. X. He *et al.*, Size distribution of water-soluble metals in atmospheric particles in Xi'an, China: Seasonal variations, bioavailability, and health risk assessment. *Atmos. Pollut. Res.* **12**, 101090 (2021).
61. California Air Resources Board, Camp Fire Air Quality Data Analysis (2021).
62. A. Singh, P. Pant, F. D. Pope, Air quality during and after festivals: Aerosol concentrations, composition and health effects. *Atmos. Res.* **227**, 220–232 (2019).
63. V. Di Marco *et al.*, Metal ion release from fine particulate matter sampled in the po valley to an aqueous solution mimicking fog water: Kinetics and solubility. *Aerosol Air Qual. Res.* **20**, 720–729 (2020).
64. N. Chatterjee, M. Flury, Effect of particle shape on capillary forces acting on particles at the air-water interface. *Langmuir* **29**, 7903–7911 (2013).
65. Q. Ma, Y. Liu, C. Liu, H. He, Heterogeneous reaction of acetic acid on MgO, α -Al₂O₃, and CaCO₃ and the effect on the hygroscopic behaviour of these particles. *Phys. Chem. Chem. Phys.* **14**, 8403–8409 (2012).
66. J. Mettakoonpitak, J. Volckens, C. S. Henry, Janus electrochemical paper-based analytical devices for metals detection in aerosol samples. *Anal. Chem.* **92**, 1439–1446 (2020).
67. R. J. Weber *et al.*, A particle-into-liquid collector for rapid measurement of aerosol bulk chemical composition. *Aerosol Sci. Technol.* **35**, 718–727 (2001).
68. B. T. Cartledge, A. R. Marcotte, P. Herckes, A. D. Anbar, B. J. Majestic, The impact of particle size, relative humidity, and sulfur dioxide on iron solubility in simulated atmospheric marine aerosols. *Environ. Sci. Technol.* **49**, 7179–7187 (2015).
69. F. Rueda-Holgado *et al.*, Miniaturized voltammetric stripping on screen printed gold electrodes for field determination of copper in atmospheric deposition. *Talanta* **101**, 435–439 (2012).
70. M. Li, H. Gou, I. Al-Ogaidi, N. Wu, Nanostructured sensors for detection of heavy metals: A review. *ACS Sustain. Chem. Eng.* **1**, 713–723 (2013).
71. P. Kampalanonwat, P. Supaphol, Preparation and adsorption behavior of aminated electrospun polyacrylonitrile nanofiber mats for heavy metal ion removal. *ACS Appl. Mater. Interfaces* **2**, 3619–3627 (2010).
72. R. Zhao *et al.*, Preparation of phosphorylated polyacrylonitrile-based nanofiber mat and its application for heavy metal ion removal. *J. Chem. Eng.* **268**, 290–299 (2015).
73. M. P. Romano *et al.*, Development and characterization of a gold nanoparticles glassy carbon modified electrode for dithiothreitol (DTT) detection suitable to be applied for determination of atmospheric particulate oxidative potential. *Anal. Chim. Acta* **1206**, 339556 (2022).
74. Z. Zou *et al.*, Environmentally friendly disposable sensors with microfabricated on-chip planar bismuth electrode for in situ heavy metal ions measurement. *Sens. Actuators B Chem.* **134**, 18–24 (2008).
75. W. C. Hinds, "Aerosol Technology: Properties, Behavior, and Measurement of Airborne Particles" (John Wiley & Sons, 1999).
76. V. A. Marple *et al.*, Next generation pharmaceutical impactor (a new impactor for pharmaceutical inhaler testing). Part I: Design. *J. Aerosol Med.* **16**, 283–299 (2003).
77. C.-N. Liu, A. Awasthi, Y.-H. Hung, C.-J. Tsai, Collection efficiency and interstage loss of nanoparticles in micro-orifice-based cascade impactors. *Atmos. Environ.* **69**, 325–333 (2013).
78. S. Taghvaei, A. Mousavi, M. H. Sowlat, C. Sioutas, Development of a novel aerosol generation system for conducting inhalation exposures to ambient particulate matter (PM). *Sci. Total Environ.* **665**, 1035–1045 (2019).
79. C. W. J. Berendsen, J. C. H. Zeegers, G. C. F. L. Kruijs, M. Riepen, A. A. Darhuber, Rupture of thin liquid films induced by impinging air-jets. *Langmuir* **28**, 9977–9985 (2012).